

## LARGE-SCALE DYNAMOS IN RIGIDLY ROTATING TURBULENT CONVECTION

PETRI J. KÄPYLÄ<sup>1</sup>, MAARIT J. KORPI<sup>1</sup>, AND AXEL BRANDENBURG<sup>2</sup>

<sup>1</sup> Observatory, University of Helsinki, P.O. Box 14, FI-00014 University of Helsinki, Helsinki, Finland; [petri.kapyla@helsinki.fi](mailto:petri.kapyla@helsinki.fi)

<sup>2</sup> NORDITA, AlbaNova University Center, Roslagstullsbacken 23, SE-10691 Stockholm, Sweden

Received 2008 December 22; accepted 2009 March 23; published 2009 May 8

### ABSTRACT

The existence of large-scale dynamos in rigidly rotating turbulent convection without shear is studied using three-dimensional numerical simulations of penetrative rotating compressible convection. We demonstrate that rotating convection in a Cartesian domain can drive a large-scale dynamo even in the absence of shear. The large-scale field contains a significant fraction of the total field in the saturated state. The simulation results are compared with one-dimensional mean-field dynamo models where turbulent transport coefficients, as determined using the test field method, are used. The reason for the absence of large-scale dynamo action in earlier studies is shown to be due to the rotation being too slow: whereas the  $\alpha$ -effect can change sign, its magnitude stays approximately constant as a function of rotation, and the turbulent diffusivity decreases monotonically with increasing rotation. Only when rotation is rapid enough a large-scale dynamo can be excited. The one-dimensional mean-field model with dynamo coefficients from the test-field results predicts reasonably well the dynamo excitation in the direct simulations. This result further validates the test field procedure and reinforces the interpretation that the observed dynamo is driven by a turbulent  $\alpha$ -effect. This result demonstrates the existence of an  $\alpha$ -effect and an  $\alpha^2$ -dynamo with natural forcing.

*Key words:* convection – MHD – stars: magnetic fields – Sun: magnetic fields – turbulence

*Online-only material:* color figures

### 1. INTRODUCTION

Convective instability drives turbulence in the outer layers of late-type stars, such as the Sun. The large-scale magnetic fields of these stars are thought to arise from the interaction of turbulent convection and the overall rotation of the object. In mean-field dynamo theory (e.g., Moffatt 1978; Parker 1979; Krause & Rädler 1980; Rüdiger & Hollerbach 2004), this process relies on large-scale differential rotation ( $\Omega$ -effect) producing toroidal field by shearing and the  $\alpha$ -effect which regenerates the poloidal field. In simple situations, the  $\alpha$ -effect is related to the kinetic helicity of the flow (e.g., Steenbeck & Krause 1969). Dynamos where differential rotation is important, e.g., the solar dynamo, are therefore often called  $\alpha\Omega$ -dynamos.

The  $\alpha\Omega$  dynamo process was first invoked by Parker (1955) to explain solar magnetism. Mean-field models have been used extensively ever since to study various aspects of dynamos. Although very useful in their own right, these models often rely on ill-known parameterizations of turbulence, such as the  $\alpha$ -effect and turbulent diffusivity. Only during recent years numerical simulations have reached a level of sophistication where large-scale  $\alpha\Omega$ -dynamos have been obtained self-consistently within the framework of local Cartesian simulations. These simulations operate in highly simplified situations and the turbulence is driven by external forcing (e.g., Brandenburg et al. 2001; Brandenburg & Käpylä 2007; Käpylä & Brandenburg 2009). In rapidly rotating stars differential rotation is likely to play only a minor role (e.g., Hall 1991) and there the  $\alpha$ -effect also generates the toroidal field. These systems are called  $\alpha^2$ -dynamos. Again, such solutions have been found from direct simulations of forced turbulence (Brandenburg 2001; Mitra et al. 2009b, 2009c).

On the other hand, numerical simulations of magnetoconvection have been around for at least two decades, but somewhat surprisingly large-scale dynamos were not found until quite recently (Jones & Roberts 2000; Rotvig & Jones 2002; Browning

et al. 2006; Brown et al. 2007; Käpylä et al. 2008, hereafter Paper I; Hughes & Proctor 2009). The first two studies are related to the geodynamo and therefore convection is rotationally dominated. The next two use a global models with an imposed tachocline (Browning et al. 2006) or rapid rotation (Brown et al. 2007), respectively. The last two are local models with imposed shear flows, reminiscent of the shear dynamos reported from nonhelical turbulence (Yousef et al. 2008a, 2008b; Brandenburg et al. 2008). The origin of large-scale fields in the nonhelically forced simulations cannot be due to the mean-field  $\alpha$ -effect. However, the incoherent  $\alpha$ -shear dynamo (e.g., Vishniac & Brandenburg 1997; Proctor 2007) or the mean-field shear-current effect (Rogachevskii & Kleeorin 2003, 2004; Kleeorin & Rogachevskii 2008) could drive these dynamos. In the shearing local convection simulations the same two effects have been suggested mainly due to the fact that rotating convection alone has so far been found unable to generate large-scale magnetic fields (e.g., Nordlund et al. 1992; Brandenburg et al. 1996; Cattaneo & Hughes 2006; Tobias et al. 2008), although it should produce a mean  $\alpha$ -effect according to theory. This drawback has prompted speculations that the  $\alpha$ -effect in its mean-field incarnation simply does not work (Hughes & Proctor 2009).

A conclusive proof of the existence of an  $\alpha^2$ -dynamo should be the demonstration of large-scale dynamo action in a simulation without shear. An additional property of such a setup is that the Vishniac & Cho (2001) flux of magnetic helicity is absent. This might lead to slow saturation of the large-scale magnetic field, unless there are other ways of shedding small-scale magnetic helicity.

The most natural way of explaining the large-scale magnetic fields seen in the rapidly rotating global convection simulations (Brown et al. 2007) would be in terms of a mean-field  $\alpha^2$ - or  $\alpha\Omega$ -dynamo. In the global models large-scale shear flows can also be generated, so it is not straightforward to determine what type of dynamo is operating there. In the present study, we use local simulations to demonstrate that large-scale dynamos

can indeed be excited in rapidly rotating convection, i.e., in the absence of shear, as long as rotation is rapid enough. We determine the turbulent transport coefficients from the simulations using the test field procedure (Schrinner et al. 2005, 2007) and use them in a one-dimensional dynamo model to test their consistency with the direct simulations. A more thorough study of the turbulent transport coefficients from convection using the test field method is presented elsewhere (Käpylä et al. 2009, hereafter Paper II).

## 2. THE MODEL

Our model setup is similar to that used by Brandenburg et al. (1996), Ossendrijver et al. (2001, 2002), Käpylä et al. (2004, 2006), and those in Papers I and II. A rectangular portion of a star is modeled by a box situated at colatitude  $\theta$ . The box is divided into three layers, an upper cooling layer, a convectively unstable layer, and a stable overshoot layer (see below). The following set of equations for compressible magnetohydrodynamics is being solved:

$$\frac{\partial \mathbf{A}}{\partial t} = \mathbf{U} \times \mathbf{B} - \eta \mu_0 \mathbf{J}, \quad (1)$$

$$\frac{D \ln \rho}{Dt} = -\nabla \cdot \mathbf{U}, \quad (2)$$

$$\frac{D\mathbf{U}}{Dt} = -\frac{1}{\rho} \nabla p + \mathbf{g} - 2\Omega \times \mathbf{U} + \frac{1}{\rho} \mathbf{J} \times \mathbf{B} + \frac{1}{\rho} \nabla \cdot 2\nu \rho \mathbf{S}, \quad (3)$$

$$\frac{De}{Dt} = -\frac{p}{\rho} \nabla \cdot \mathbf{U} + \frac{1}{\rho} \nabla \cdot K \nabla T + 2\nu \mathbf{S}^2 + \frac{\eta}{\rho} \mu_0 \mathbf{J}^2 - \frac{e - e_0}{\tau(z)}, \quad (4)$$

where  $D/Dt = \partial/\partial t + \mathbf{U} \cdot \nabla$ . The magnetic field is written in terms of the magnetic vector potential,  $\mathbf{A}$ , with  $\mathbf{B} = \nabla \times \mathbf{A}$ ,  $\mathbf{J} = \mu_0^{-1} \nabla \times \mathbf{B}$  is the current density,  $\mu_0$  is the vacuum permeability,  $\eta$  and  $\nu$  are the magnetic diffusivity and kinematic viscosity, respectively,  $K$  is the heat conductivity,  $\rho$  is the density,  $\mathbf{U}$  is the velocity,  $\mathbf{g} = -g\hat{\mathbf{z}}$  is the gravitational acceleration, and  $\Omega = \Omega_0(-\sin\theta, 0, \cos\theta)$  is the rotation vector. The fluid obeys an ideal gas law  $p = (\gamma - 1)\rho e$ , where  $p$  and  $e$  are pressure and internal energy, respectively, and  $\gamma = c_p/c_v = 5/3$  is the ratio of specific heats at constant pressure and volume, respectively. The specific internal energy per unit mass is related to the temperature via  $e = c_v T$ . The rate of strain tensor  $\mathbf{S}$  is given by

$$\mathbf{S}_{ij} = \frac{1}{2}(U_{i,j} + U_{j,i}) - \frac{1}{3}\delta_{ij} \nabla \cdot \mathbf{U}. \quad (5)$$

The last term of Equation (4) describes cooling at the top of the domain. Here,  $\tau(z)$  is a cooling time which has a profile smoothly connecting the upper cooling layer and the convectively unstable layer below, where  $\tau \rightarrow \infty$ .

The positions of the bottom of the box, bottom and top of the convectively unstable layer, and the top of the box, respectively, are given by  $(z_1, z_2, z_3, z_4) = (-0.85, 0, 1, 1.15)d$ , where  $d$  is the depth of the convectively unstable layer. Initially, the stratification is piecewise polytropic with polytropic indices  $(m_1, m_2, m_3) = (3, 1, 1)$ , which leads to a convectively unstable layer above a stable layer at the bottom of the domain. The cooling term leads to a stably stratified isothermal layer at the top. The horizontal extent of the box  $L_H \equiv L_x = L_y$  is varied between  $2d$  and  $8d$ . All simulations with rotation use  $\theta = 0^\circ$  corresponding to the north pole.

### 2.1. Units and Nondimensional Parameters

Nondimensional quantities are obtained by setting

$$d = g = \rho_0 = c_p = \mu_0 = 1, \quad (6)$$

where  $\rho_0$  is the initial density at  $z_2$ . The units of length, time, velocity, density, entropy, and magnetic field are

$$\begin{aligned} [x] &= d, & [t] &= \sqrt{d/g}, & [U] &= \sqrt{dg}, & [\rho] &= \rho_0, \\ [s] &= c_p, & [B] &= \sqrt{dg\rho_0\mu_0}. \end{aligned} \quad (7)$$

We define the fluid and magnetic Prandtl numbers and the Rayleigh number as

$$\text{Pr} = \frac{\nu}{\chi_0}, \quad \text{Pm} = \frac{\nu}{\eta}, \quad \text{Ra} = \frac{gd^4}{\nu\chi_0} \left( -\frac{1}{c_p} \frac{ds}{dz} \right)_0, \quad (8)$$

where  $\chi_0 = K/(\rho_m c_p)$  is the thermal diffusivity, and  $\rho_m$  is the density in the middle of the unstable layer,  $z_m = \frac{1}{2}(z_3 - z_2)$ . The entropy gradient, measured at  $z_m$ , in the nonconvecting hydrostatic state, is given by

$$\left( -\frac{1}{c_p} \frac{ds}{dz} \right)_0 = \frac{\nabla - \nabla_{\text{ad}}}{H_p}, \quad (9)$$

where  $\nabla - \nabla_{\text{ad}}$  is the superadiabatic temperature gradient with  $\nabla_{\text{ad}} = 1 - 1/\gamma$ ,  $\nabla = (\partial \ln T / \partial \ln p)_{z_m}$ , and where  $H_p$  is the pressure scale height (Brandenburg et al. 2005). The amount of stratification is determined by the parameter  $\xi_0 = (\gamma - 1)e_0/(gd)$ , which is the pressure scale height at the top of the domain normalized by the depth of the unstable layer. We use  $\xi_0 = 1/3$  in all cases, which results in a density contrast of about 23 across the domain. We define the fluid and magnetic Reynolds numbers via

$$\text{Re} = \frac{u_{\text{rms}}}{\nu k_f}, \quad \text{Rm} = \frac{u_{\text{rms}}}{\eta k_f} = \text{Pm Re}, \quad (10)$$

where  $k_f = 2\pi/d$  is adopted as an estimate for the wavenumber of the energy-carrying eddies. Note that with our definition  $\text{Rm}$  is smaller than the usual one by a factor  $2\pi$ . The amount of rotation is quantified by

$$\text{Co} = \frac{2\Omega_0}{u_{\text{rms}} k_f}. \quad (11)$$

In order to facilitate comparison with earlier studies of rotating Rayleigh–Bénard convection, we also quote the value of the Taylor number,

$$\text{Ta} = (2\Omega_0 d^2 / \nu)^2 = (4\pi^2 \text{Co Rm} / \text{Pm})^2. \quad (12)$$

The equipartition magnetic field is defined by

$$B_{\text{eq}} \equiv (\mu_0 \rho U^2)^{1/2}, \quad (13)$$

where angular brackets denote volume averaging.

### 2.2. Boundary Conditions

Stress-free boundary conditions are used in the vertical ( $z$ ) direction for the velocity,

$$U_{x,z} = U_{y,z} = U_z = 0, \quad (14)$$

**Table 1**  
Summary of the Runs

Run	Grid	$L_H$	Pr	Pm	Ra	Rm	Co	Ta	Ma	$\tilde{B}_{\text{rms}}$	$\tilde{B}^{(0)}$	$\tilde{B}^{(1)}$	BC
A1	$128^3$	2	0.27	2	$1.5 \times 10^6$	70	0	0	0.044	0.12	0.02	0.05	VF
A2	$128^3$	2	0.27	2	$1.5 \times 10^6$	68	0.37	$2.5 \times 10^5$	0.043	0.23	0.04	0.10	VF
A3	$128^3$	2	0.27	2	$1.5 \times 10^6$	68	0.74	$10^6$	0.043	0.25	0.04	0.09	VF
A4	$128^3$	2	0.27	2	$1.5 \times 10^6$	69	1.5	$4 \times 10^6$	0.043	0.14	0.02	0.05	VF
A5	$128^3$	2	0.27	2	$1.5 \times 10^6$	62	4.1	$2.5 \times 10^7$	0.039	0.18	0.04	0.07	VF
A6	$128^3$	2	0.27	2	$1.5 \times 10^6$	42	11.6	$10^8$	0.028	0.38	<b>0.22</b>	<b>0.18</b>	VF
A7	$128^3$	2	0.27	1	$1.5 \times 10^6$	22	11.6	$10^8$	0.028	0.27	<b>0.15</b>	<b>0.16</b>	VF
A8	$128^3$	2	0.27	0.67	$1.5 \times 10^6$	17	9.8	$10^8$	0.033	0.00	0.00	0.00	VF
A9	$128^3$	2	0.27	0.4	$1.5 \times 10^6$	10	9.7	$10^8$	0.033	0.00	0.00	0.00	VF
A10	$256^3$	2	0.14	2	$3.0 \times 10^6$	107	9.5	$4 \times 10^8$	0.034	0.41	<b>0.08</b>	<b>0.15</b>	VF
B1	$256^2 \times 128$	4	0.27	2	$1.5 \times 10^6$	77	0	0	0.048	0.22	0.02	0.06	VF
B2	$256^2 \times 128$	4	0.27	2	$1.5 \times 10^6$	67	0.38	$2.5 \times 10^5$	0.042	0.25	0.02	0.05	VF
B3	$256^2 \times 128$	4	0.27	2	$1.5 \times 10^6$	66	0.76	$10^6$	0.042	0.22	0.02	0.05	VF
B4	$256^2 \times 128$	4	0.27	2	$1.5 \times 10^6$	67	1.5	$4 \times 10^6$	0.042	0.16	0.01	0.03	VF
B5	$256^2 \times 128$	4	0.27	2	$1.5 \times 10^6$	55	4.6	$2.5 \times 10^7$	0.035	0.31	0.05	0.09	VF
B6	$256^2 \times 128$	4	0.27	2	$1.5 \times 10^6$	42	11.9	$10^8$	0.027	0.41	<b>0.12</b>	<b>0.15</b>	VF
B7	$256^2 \times 128$	4	0.27	2	$1.5 \times 10^6$	41	12.4	$10^8$	0.026	0.48	<b>0.18</b>	<b>0.26</b>	PC
C1	$512^2 \times 128$	8	0.27	2	$1.5 \times 10^6$	42	12.0	$10^8$	0.026	0.45	<b>0.07</b>	<b>0.17</b>	VF
D1	$512^2 \times 256$	4	0.14	2	$3.0 \times 10^6$	97	10.5	$4 \times 10^8$	0.030	0.58	<b>0.08</b>	<b>0.30</b>	VF

**Notes.** Here,  $\text{Ma} = u_{\text{rms}}/(gd)^{1/2}$ ,  $\tilde{B}_{\text{rms}} \equiv B_{\text{rms}}/B_{\text{eq}}$ , and the  $\tilde{B}^{(k)}$  are the sum of the rms values of the Fourier amplitudes of the horizontal components of the magnetic field for mode  $k$  normalized by  $B_{\text{rms}}$ . Values with  $\tilde{B}^{(0)} \geq 0.07$  or  $\tilde{B}^{(1)} \geq 0.15$  are shown in bold face and indicate the presence of significant large-scale fields. The last column denotes the magnetic field boundary condition at the  $z$ -boundaries.

where commas denote partial derivatives, and either vertical field (VF) of perfect conductor (PC) conditions are used for the magnetic field, i.e.,

$$B_x = B_y = 0 \quad (\text{vertical field}), \quad (15)$$

$$B_{x,z} = B_{y,z} = B_z = 0 \quad (\text{perfect conductor}). \quad (16)$$

The VF conditions permit a magnetic helicity flux, but no Poynting flux, whereas the PC conditions do not allow helicity fluxes either. In the  $x$  and  $y$  directions periodic boundary conditions are used. The simulations were made with the PENCIL CODE,<sup>3</sup> which uses sixth-order explicit finite differences in space and third-order accurate time stepping method. Resolutions of up to  $512^2 \times 256$  mesh points were used.

### 3. RESULTS

We perform a parameter study where we vary the system size, the effect of rotation, quantified by Co, and the Reynolds numbers in order to study the existence of large-scale dynamo in rotating convection. The runs are listed in Table 1. We briefly describe the hydrodynamics of these runs in Section 3.1, and the results on dynamo excitation and large-scale magnetic fields are given in Section 3.2. Finally, in Sections 3.3 and 3.4 the turbulent transport coefficients and the interpretation of the results in the framework of mean-field electrodynamics, respectively, are presented.

#### 3.1. The Hydrodynamic State

All our simulations start with a small (of the order of  $10^{-5} B_{\text{eq}}$ ) random magnetic field. This field remains dynamically insignificant in the initial stages, which, in most cases, span the first 200 turnover times of the run. As in Paper I, we

consider this interval to represent the hydrodynamic state of the simulation.

The effect of rotation on convection has been described in various papers (e.g., Käpylä et al. 2004; Giesecke et al. 2005; Cattaneo & Hughes 2006; Hughes & Cattaneo 2008; Tobias et al. 2008). The most visible effect is the decreasing size of convective cells as rotation is increased, see Figure 1. Without rotation (Run B1) and for horizontal extent  $L_H/d = 4$  the flow is dominated by essentially a single large cell, but already for  $\text{Co} \approx 1.5$  (Run B4) there are of the order of 10 or more cells in the domain. When rotation is increased further, the cell size continues to diminish. This feature is familiar from simulations of unstratified convection (King et al. 2009), although there the flow appears to become more easily laminar at large Taylor numbers ( $\text{Ta} = 10^8$ ) and modestly large Rayleigh numbers ( $\text{Ra} = 1.5 \times 10^6$ ) that we used here (see Table 1).

The decrease in cell size is also manifested by two-dimensional power spectra of the velocity, see the upper panel of Figure 2. For the nonrotating case (Run B1), the most power is found at  $k/k_1 = 1$ , where  $k_1 = 2\pi/L_H$ . There is a tendency for the wavenumber of the maximum,  $k_{\text{max}}$ , to shift toward higher  $k$  for more rapid rotation. The lower panel of Figure 2 shows the velocity power spectra for Runs A6, B6, and C1 with  $L_H/d = 2, 4, 8$ , respectively, shifted so that the same spatial scales coincide. All runs have  $\text{Re} \approx 28$  (21) and  $\text{Co} \approx 9$  (12) in the kinematic (saturated) regime. For the smallest system size the energy still peaks near the box scale. When the box size increases the spatial scale at which most energy is found stays the same and, as a consequence, the scale separation,  $k_{\text{max}}/k_1$ , between the energy-carrying scale and the box scale increases.

Our finding that  $k_{\text{max}}$  is independent of the horizontal system size is important because large-scale dynamo require some amount of scale separation, i.e., that the power spectrum of the turbulence should peak at some scale smaller than the

<sup>3</sup> <http://www.nordita.org/software/pencil-code/>

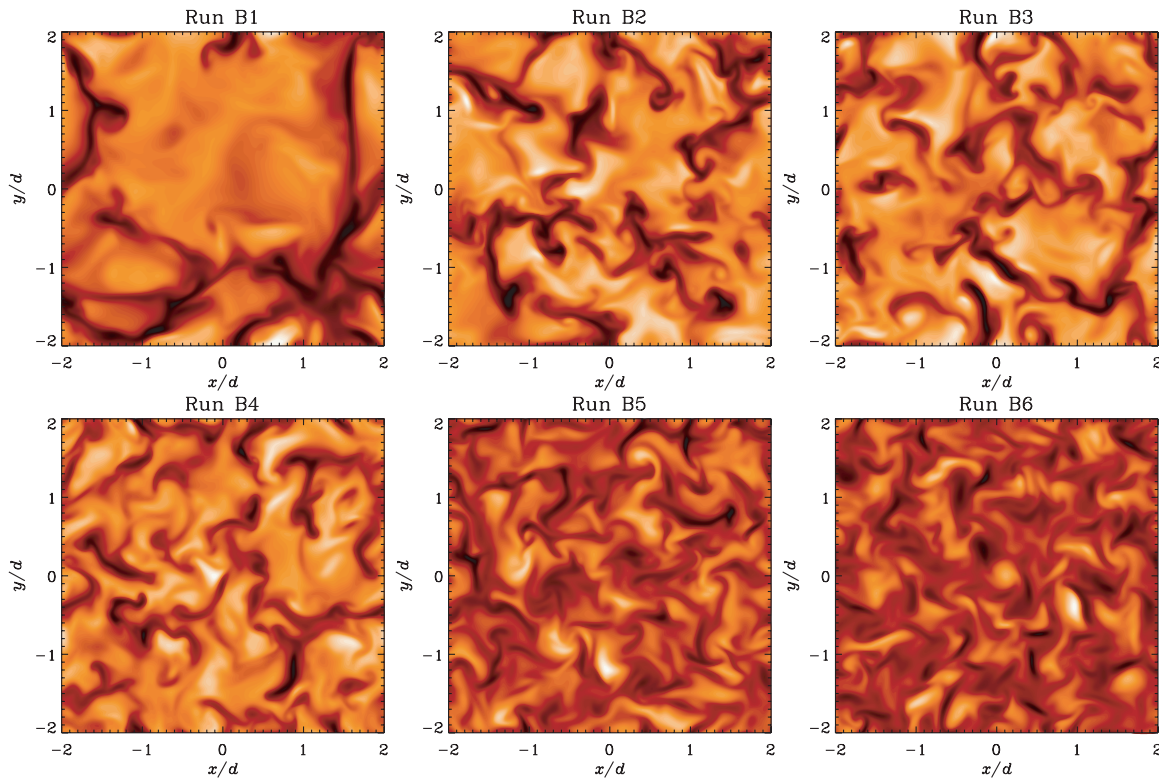


**Figure 1.** Vertical velocity  $U_z$  from the middle of the convectively unstable layer from Runs B1 to B6 in the kinematic stage at  $t = 400\sqrt{d/g}$ , corresponding to  $tu_{\text{rms}}k_t \approx 70, \dots, 110$ , depending on the run. Light (dark) color indicates ascending (descending) motion.

(A color version of this figure is available in the online journal.)

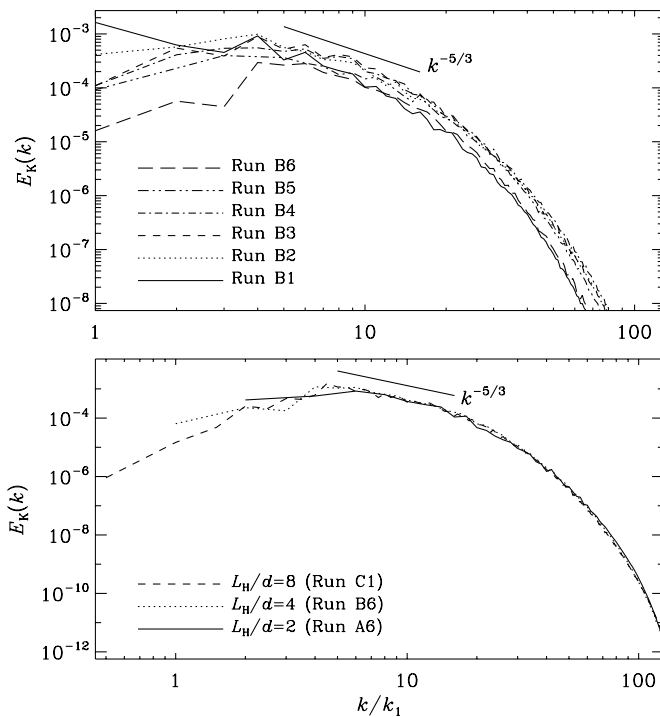


**Figure 2.** Two-dimensional power spectra of velocity from the middle of the convectively unstable layer as functions of rotation (upper panel) and system size (lower panel) in the kinematic regime at  $t = 400\sqrt{d/g}$ . Power-law slopes proportional to  $k^{-5/3}$  are shown for reference. The spectra in the lower panel have been shifted so that the same spatial scales coincide on the  $x$ -axis and scaled by  $L_H/d$  so that the curves lie on top of each other.

system size. This allows the energy to cascade to smaller and larger scales. The former eventually dissipates the energy into heat whereas the latter can generate large-scale structures through an inverse cascade of energy. The turbulent  $\alpha$ -effect can also be interpreted as an inverse cascade (Brandenburg 2001). If, however, the flow energy peaks at, or close to, the scale of the system, it is impossible to cascade energy to larger scales.

### 3.2. Dynamo Excitation and Large-scale Magnetic Fields

Recent numerical studies have indicated that shear plays an important role in exciting large-scale dynamos (e.g., Yousef et al. 2008a, 2008b; Paper I; Hughes & Proctor 2009). Although the process generating the large-scale magnetic field in the nonhelical case is still under debate (e.g., Rogachevskii & Kleeorin 2003, 2004; Rüdiger & Kitchatinov 2006; Proctor 2007; Brandenburg et al. 2008; Schekochihin et al. 2009; Sridhar & Subramanian 2009), there are some indications that in helical turbulence with shear a classical  $\alpha\Omega$ , or  $\alpha$ -shear dynamo, simultaneously with a shear-current and  $\Omega \times \mathbf{J}$ -dynamos, might be the explanation (Paper II). However, in the absence of shear, large-scale dynamos due to helical turbulence have so far been obtained only in idealized systems where the helical flow is driven by external forcing (Brandenburg 2001; Mitra et al. 2009b, 2009c). In particular, the lack of large-scale dynamos in rotating convection has been puzzling (e.g., Cattaneo & Hughes 2006), although an  $\alpha$ -effect should be present according to theory. One possible explanation is that, whereas the turbulence in more idealized studies can be

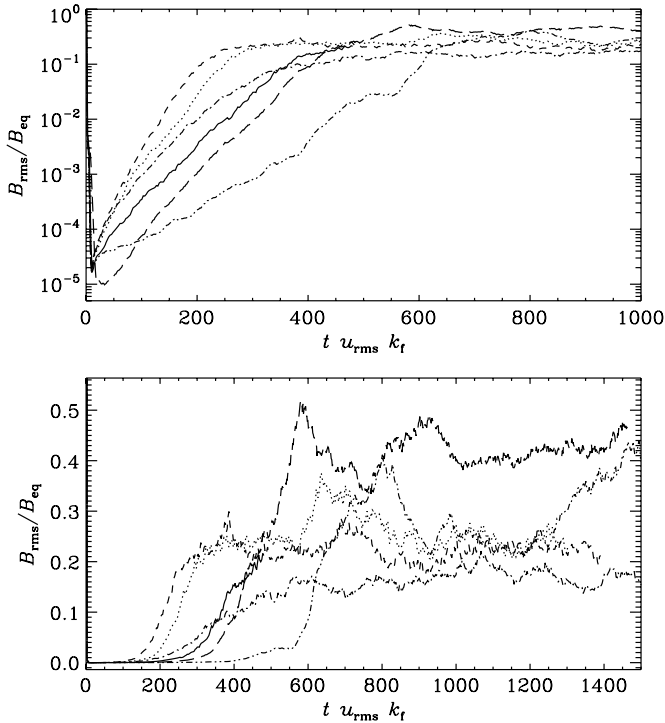


**Figure 3.** Upper panel: rms of the total magnetic field as a function of time for the same runs as in the upper panel of Figure 2. Lower panel: the same as above but in linear scale.

almost fully helical owing to the forcing, in rotating convection the fractional helicity is often much smaller (e.g., Brandenburg et al. 1990, 1996; Käpylä et al. 2004).

In Paper II, we found that the turbulent  $\alpha$ -effect increases and turbulent diffusivity decreases, respectively, as functions of rotation for small fluid Reynolds numbers (see below). These results suggest that a large-scale dynamo in rotating convection is excited only if rotation is rapid enough. Our conjecture is that this regime might not have been reached in earlier studies thus failing to produce large-scale dynamos.

The evolution of the rms value of the total magnetic field for Runs B1–B6 is shown in Figure 3. We find that the growth rate of the field increases for  $\text{Co} \lesssim 0.74$  (Runs B1–B3) after which it starts to decrease. However, for the most rapid rotation (Run B6) the growth rate again increases and is close to the nonrotating case. The saturation level of the magnetic field is practically constant for  $\text{Co} \lesssim 0.74$  (Runs B1–B3) and somewhat lower for  $\text{Co} \approx 1.5$  (Run B4). For the two most rapidly rotating cases the saturation level is generally higher and more variable. In these runs, the maxima of the field are associated with periods where significant amounts of large-scale fields are present; see Figure 4 for the time evolution of horizontally averaged fields  $\bar{B}_x$  and  $\bar{B}_y$  for Run A6. Comparing the field in the kinematic and saturated stages (Figure 5) shows that in the kinematic regime the field is concentrated in small scales, whereas in the late stages a clear large-scale structure is visible. The behavior of the growth rate and saturation level of the field as functions of rotation could be understood as follows: the small-scale dynamo is enhanced for slow rotation but starts to be rotationally quenched for  $\text{Co} \gtrsim 1$ . This might be explicable by an associated decrease in the length scale of the turbulence. On the other hand, for rapid enough rotation, i.e.,  $\text{Co} \gtrsim 3$ , the large-scale dynamo becomes excited and increases the growth rate and saturation level. We stress that the proposed suppression of the small-scale dynamo action due

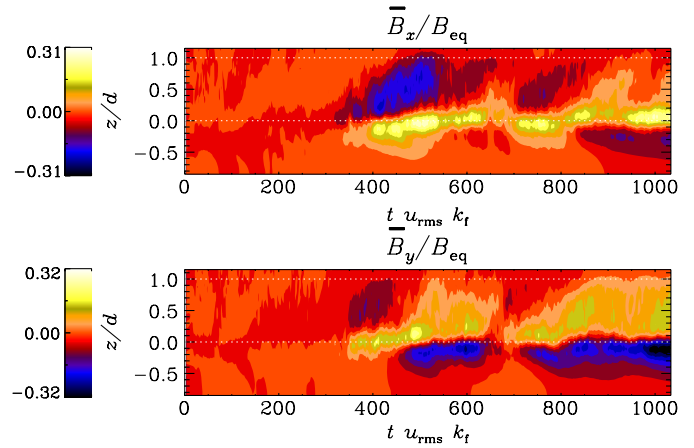


**Figure 4.** Horizontally averaged magnetic field components  $\bar{B}_x$  (top panel) and  $\bar{B}_y$  (bottom panel), normalized by the equipartition magnetic field strength. From Run A6 with  $\text{Co} \approx 12$  and  $\text{Rm} \approx 42$ . The horizontal dotted lines at  $z/d = 0$  and  $z/d = 1$  indicate the base and top of the convectively unstable layer, respectively.

(A color version of this figure is available in the online journal.)

to rotation is at this stage only a conjecture that is consistent with the numerical data. Whether this interpretation is correct should be studied in more detail separately. It should also be noted that we cannot expect rotation to quench the small-scale dynamo in the astrophysically relevant regime where  $\text{Rm}$  is much larger than in the present simulations. There are, however, no compelling reasons to expect that the large-scale dynamo is suppressed when a small-scale dynamo is also present as long as magnetic helicity fluxes are allowed to leave the domain. For the most rapidly rotating case, with  $\text{Co} \approx 9$  in the kinematic regime, the critical magnetic Reynolds number is roughly 20, see Figure 6. In Paper I, we reported that in the absence of rotation, the critical  $\text{Rm}$  for the excitation of a small-scale dynamo is roughly 30 for a similar system.

In Paper I, we found the large-scale field to be dominated by the  $k_x = k_y = 0$  mode and it could thus be well described by a horizontal average. However, in the present case the mean fields show a more complicated structure and tend to have comparable contributions from  $k_x, k_y \neq 0$  modes as well (see, e.g., the right panel of Figure 5). Thus, a simple horizontal average no longer suffices to represent the large-scale field. For a better measure, we perform a two-dimensional Fourier transform of the field at each horizontal layer, the result of which we denote by  $\hat{B}_i(k_x, k_y, z, t)$ . Now, we project this quantity onto a one-dimensional wavenumber  $k^2 = k_x^2 + k_y^2$  and denote its Fourier amplitude by  $\hat{B}_i^{(m)}(z, t)$ , where  $m$  is the discretized wavenumber bin corresponding to  $k/k_1$ . So, for  $k/k_1 = 0$ ,  $\hat{B}_i^{(0)}(z, t)$  is the same as a horizontal average  $\bar{B}_i$ . For larger  $k$ ,  $\hat{B}_i^{(m)}(z, t)$  gives a measure of the strength of the mode  $k$ . In the following we restrict the analysis to the smallest values of  $k/k_1 = 0, \dots, 2$  that describe the large-scale field.

Representative results for the horizontal components of  $\hat{B}_i^{(0)}(z, t)$  and  $\hat{B}_i^{(1)}(z, t)$  from Run B6 with  $\text{Co} \approx 12$  are shown in Figure 7. The large-scale field seems to show opposite signs in the convectively unstable and stable layers. Sign changes also occur but they are rather irregular and do not appear to follow a consistent cycle. The rms of the amplitudes for the  $k/k_1 = 0$  and 1 contributions to the horizontal magnetic fields are of the order of 10% of the equipartition value. This is to be contrasted with Figure 8 where the sums of the rms values of

the amplitudes of the three smallest wavenumbers are shown as functions of rotation. Substantial large-scale fields are observed only for the two largest values of  $Co$ ; for  $Co \lesssim 1.5$  the runs show very weak large-scale contributions. This is also visible in the two-dimensional power spectra, taken from the middle of the convectively unstable layer, see Figure 9. The most rapidly rotating case (Run B6) is the only one showing clear signs of large-scale fields, in accordance with the fact that the large-scale field is only periodically present in Run B5. The velocity spectra in the saturated state are similar to those in the kinematic phase.

In comparison to earlier studies of rotating convection (e.g., Cattaneo & Hughes 2006; Tobias et al. 2008), we note that it is characteristic of these studies that when the Rayleigh number is increased, the Taylor number is kept constant. Increasing  $Ra$  in these models generates a larger  $u_{rms}$  and this inevitably means that the Coriolis number decreases as the Rayleigh number is increased, i.e., for a fixed  $Ta$  the rotational influence is large for a small Rayleigh number and vice versa. For example, in the paper of Cattaneo & Hughes (2006), the smallest Rayleigh numbers in combination with  $Ta = 5 \times 10^5$  gives a Coriolis number comparable to our largest values. However, these simulations do not exhibit dynamo action due to a too low  $Rm$ , whose value also depends on  $u_{rms}$ . For their highest Rayleigh number case, however,  $Rm$  is large enough for dynamo excitation but the Coriolis number is smaller by approximately an order of magnitude and no large-scale fields are observed. Similar arguments apply to the simulations of Tobias et al. (2008).

We find that the large-scale dynamo is excited for all box sizes for the most rapidly rotating case explored in the present study, as is evident from the spectra shown in Figure 10. From the spectra it would seem that an increasing amount of energy is in the large scales as the box size increases. The growth rate of the total field does not show any clear trend with the system size: the largest departure from a constant growth rate is the somewhat lower value for Run B6 with the intermediate box size (see Figure 11).

Figure 11 shows the sums of the Fourier amplitudes of the three smallest wavenumbers as functions of the system size. For the smallest box (Run A6), the large-scale field is more concentrated on the  $k/k_1 = 0$  contribution, whereas in Run B6 with  $L_H/d = 4$  the amplitudes for  $k/k_1 = 0$  and 1 are similar. For the largest domain size the  $k = 0$  mode is significantly weaker than the  $k/k_1 = 1$  and 2 modes. These results suggest

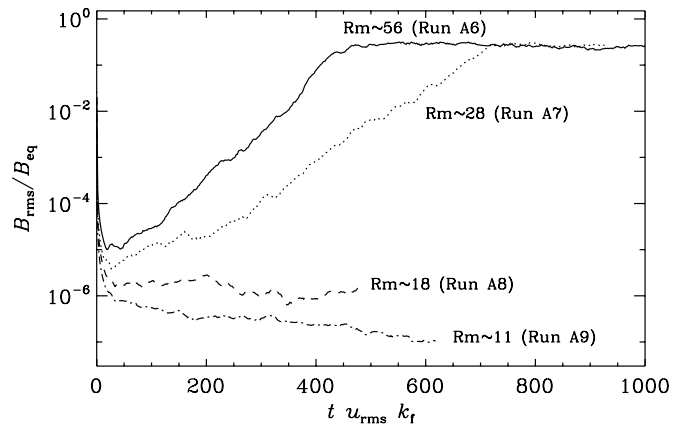


Figure 6. Root-mean-square total magnetic field as a function of time for four magnetic Reynolds numbers for Runs A6–A9.

that for the present parameters the maximum size of the large-scale structures is somewhere in the range  $2 < L_{max}/d < 8$ .

Comparing the saturation level of the large-scale magnetic field in the small box Runs A7, A6, and A10 shows a significant decrease in the  $m = 0$  component in Run A10 whereas the strength of the  $m = 1$  mode is only mildly affected. On the other hand, comparing Runs B6 and D1 with a larger domain size shows again a decreasing  $m = 0$  contribution in Run D1 but a two times larger  $m = 1$  component. However, these numbers should be taken only as a rough guide because the large-scale contribution to the magnetic field shows large fluctuations and the higher  $Rm$  runs are fairly short. Taken at face value, the results would seem to suggest that the strength of the  $m = 0$  mode decreases with increasing  $Rm$  and that the  $m = 1$  mode remains unaffected or that it can even increase. We note that the highest  $Rm$  runs also have larger fluid Reynolds and Rayleigh numbers which means that also the flow is more turbulent in those cases which could affect the dynamo and thus the saturation level of the large-scale field.

Although we have used open (VF) boundary conditions that do permit magnetic helicity fluxes, such fluxes may not actually occur unless they are driven toward the boundaries by internal magnetic helicity fluxes. One such flux is the Vishniac & Cho (2001) flux, but it requires shear which is absent in our case. Other fluxes are possible (Subramanian & Brandenburg 2006), but we do not know how efficient they are in our model. It is

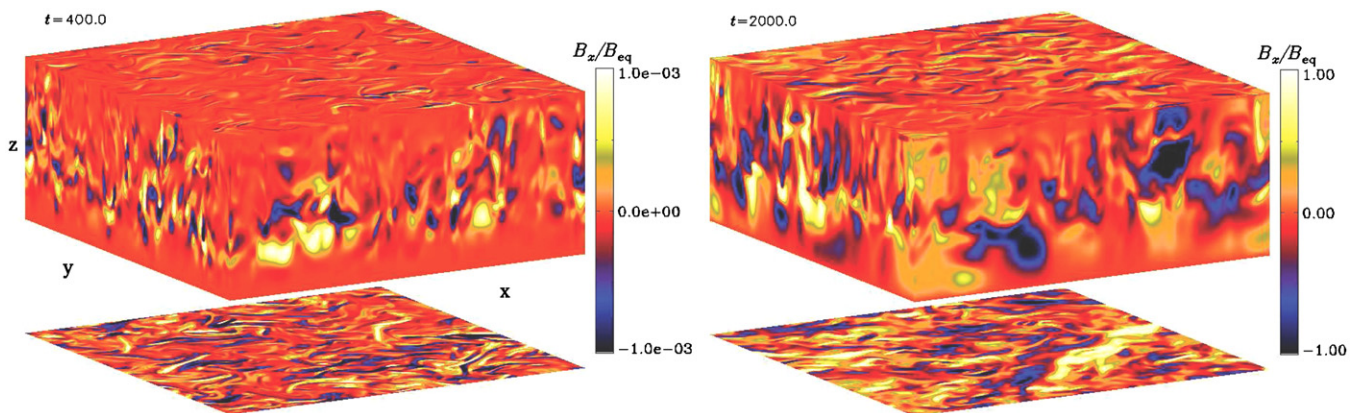
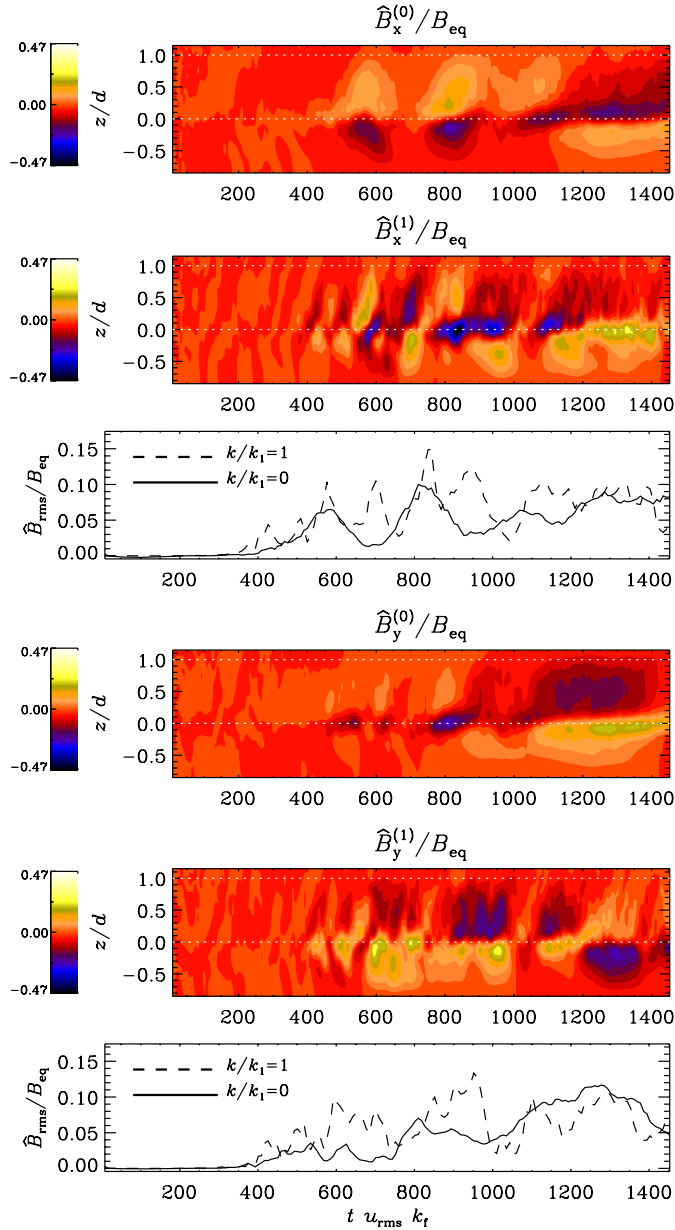


Figure 5. Magnetic field component  $B_z$  for Run D1 in the kinematic (left panel) and saturated (right) states. The sides of the box show the periphery of the domain whereas the top and bottom panels show the field from the top ( $z = d$ ) and bottom ( $z = 0$ ) of the convectively unstable layer, respectively. See also <http://www.helsinki.fi/~kapyla/movies.html>.

(A color version of this figure is available in the online journal.)



**Figure 7.** Fourier amplitudes of the two horizontal components of the magnetic field for the two smallest wavenumbers  $k/k_1 = 0$  and  $1$  from Run B6. From top to bottom:  $\hat{B}_x^{(0)}(z, t)$ ,  $\hat{B}_x^{(1)}(z, t)$ , their rms values;  $\hat{B}_y^{(0)}(z, t)$ ,  $\hat{B}_y^{(1)}(z, t)$  and their rms values.

(A color version of this figure is available in the online journal.)

therefore unclear whether one should expect the saturation of the large-scale field to occur on a dynamical or a resistive timescale, and what the relevant length scale is. In Figure 12, we show the saturation behavior for Run B6 and compare with a curve proportional to  $1 - \exp[-2\eta k^2(t - t_s)]$  that would be expected for resistively dominated saturation behavior (Brandenburg 2001). Here,  $k = k_f$  has been chosen and  $t_s$  marks the end of the linear growth phase, which is also the time when the small-scale magnetic field has saturated. The result is not entirely conclusive, and larger magnetic Reynolds number would be needed to clarify this, but it is certainly possible that saturation of the large-scale field is resistively dominated. Similar behavior is certainly expected in the case of PC boundary conditions (Run B7; see the dashed lines in Figure 12). We note that the saturation level of the total and mean fields are higher in Run B7 with

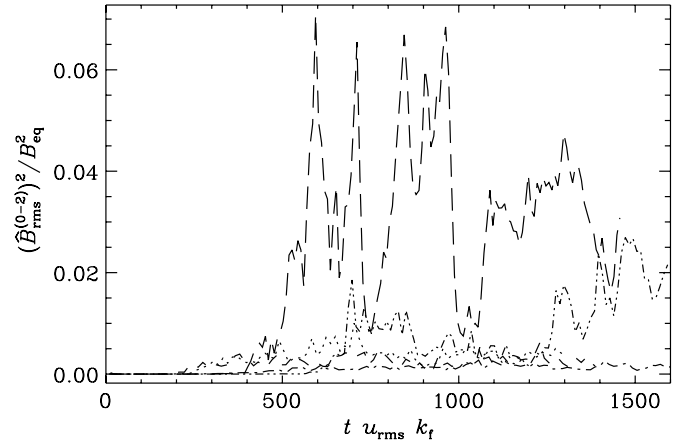


**Figure 8.** Sums of the root-mean-square values of the Fourier amplitudes of  $B_x$  and  $B_y$  for the modes  $k/k_1 = 0, \dots, 2$  as a function of rotation for the Runs B1–B6. Line styles as in the upper panel of Figure 2.

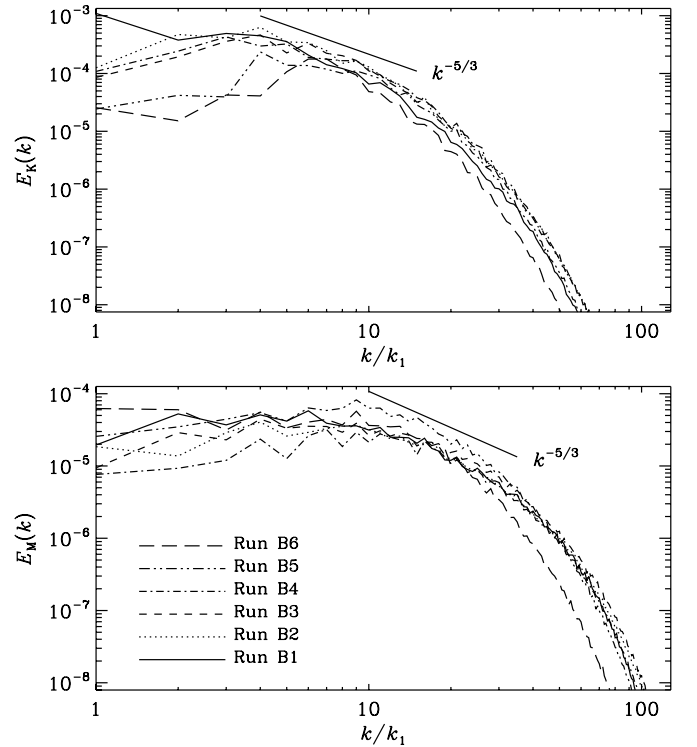


**Figure 9.** Two-dimensional power spectra of velocity (upper panel) and magnetic field (lower panel) from Runs B1 to B6 in the saturated state. Power laws proportional to  $k^{-5/3}$  are shown for reference.

PC boundary conditions than in Run B6 with VF conditions. The behavior is qualitatively similar to the forced turbulence simulations of Brandenburg (2001).

### 3.3. Turbulent Transport Coefficients

We attempt to connect the dynamos seen in the direct simulations to theoretical considerations by comparing the results to a mean-field dynamo that relies on turbulent transport coefficients, such as the  $\alpha$ -effect and turbulent diffusivity. In order to extract these coefficients, we use the test field method (Schrinner et al. 2005, 2007) in the kinematic regime. Detailed descriptions of the method, as implemented here, have been presented elsewhere (e.g., Brandenburg et al. 2008; Sur et al. 2008; Mitra et al. 2009a; Paper II); here we only outline the

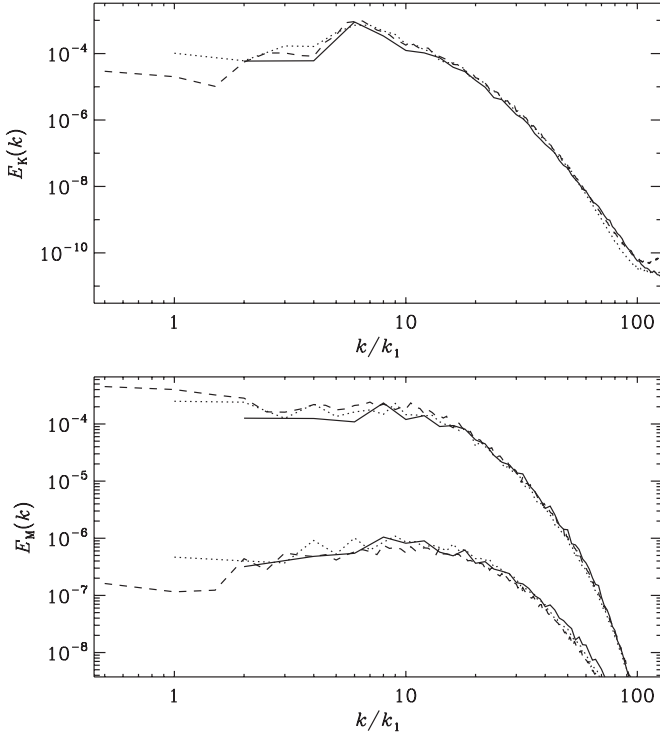


**Figure 10.** Two-dimensional power spectra of velocity (upper panel) and magnetic field (lower panel) as functions of system size. Line styles and scaling as in the lower panel of Figure 2. In the lower panel, the upper curves show the spectra from the saturated state whereas the lower curves show the spectra from the kinematic state multiplied by  $10^7$ .

general procedure. The method relies on a set of orthogonal test fields that do not evolve in time and do not react back onto the flow. These properties allow an unambiguous determination of the turbulent transport coefficients in the kinematic regime without the complications associated with some other methods that can be used.

We restrict the study to test fields that depend only on  $z$ :

$$\overline{\mathbf{B}}^{1c} = B_0(\cos kz, 0, 0), \quad \overline{\mathbf{B}}^{2c} = B_0(0, \cos kz, 0), \quad (17)$$

$$\overline{\mathbf{B}}^{1s} = B_0(\sin kz, 0, 0), \quad \overline{\mathbf{B}}^{2s} = B_0(0, \sin kz, 0), \quad (18)$$

where  $B_0$  is the amplitude of the field and  $k$  is the wavenumber of the test field. (The results are strictly independent of the value of  $B_0$ , so in nondimensional units it can be set to 1.) We use  $k/k_1 = 1$ , where  $k_1 = 2\pi/L_z$ , in all models. The  $k$ -dependence of the coefficients in convection was studied in Paper II. The electromotive force can be written as

$$\overline{\mathcal{E}}_i = \alpha_{ij} \overline{B}_j - \eta_{ij} \mu_0 \overline{J}_j, \quad (19)$$

where  $\eta_{11} = \eta_{23}$  and  $\eta_{12} = -\eta_{13}$ . The 4 + 4 coefficients are then obtained by inverting a simple matrix equation, relating the rank-2 tensor components to rank-3 tensor components.

It is convenient to discuss the results in terms of the quantities

$$\alpha = \frac{1}{2}(\alpha_{11} + \alpha_{22}), \quad \gamma = \frac{1}{2}(\alpha_{21} - \alpha_{12}), \quad (20)$$

$$\eta_t = \frac{1}{2}(\eta_{11} + \eta_{22}), \quad \delta = \frac{1}{2}(\eta_{21} - \eta_{12}). \quad (21)$$

These quantities can be understood to represent the generation of large-scale magnetic fields ( $\alpha$ ), turbulent pumping of

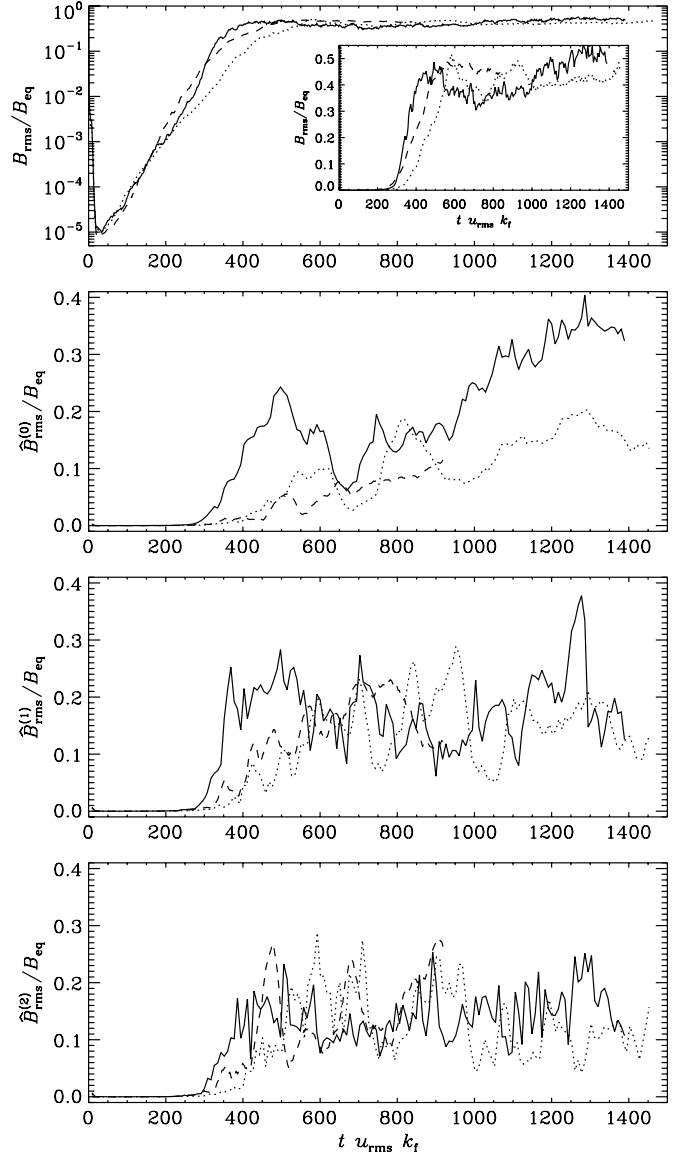


**Figure 11.** Top panel: rms values of the total magnetic field as functions of the system size. The three lower panels show the sums of the rms values of the Fourier amplitudes of  $B_x$  and  $B_y$  for  $k/k_1 = 0$  (the second panel from the top),  $k/k_1 = 1$  (second from the below), and  $k/k_1 = 2$  (bottom panel). Line styles as in the lower panel of Figure 2.

magnetic fields ( $\gamma$ ), turbulent diffusivity ( $\eta_t$ ), and the  $\Omega \times \mathbf{J}$  effect ( $\delta$ ). To normalize our results, we use isotropic expressions derived under first-order smoothing approximation (see, e.g., Paper II)

$$\alpha_0 = \frac{1}{3} u_{\text{rms}}, \quad \eta_{t0} = \frac{1}{3} u_{\text{rms}} k_f^{-1}. \quad (22)$$

Figure 13 shows the kinetic helicity  $\overline{\boldsymbol{\omega} \cdot \mathbf{u}}$ , where  $\boldsymbol{\omega} = \nabla \times \mathbf{u}$ , and the turbulent transport coefficients for Runs B2–B6 as functions of rotation. The magnetic Reynolds number varies between  $\text{Rm} \approx 58, \dots, 86$  with larger values occurring for slower rotation.  $\text{Pm} = 2$  used in all runs. These simulations differ from those in Paper II in that  $\text{Pr}$  and  $\text{Pm}$  are, respectively, five times and 2.5 times smaller. We find that the kinetic helicity increases monotonically as a function of rotation as in Paper II, although here the increase is not as steep as in the previous results. The  $\alpha$ -effect is approximately constant for

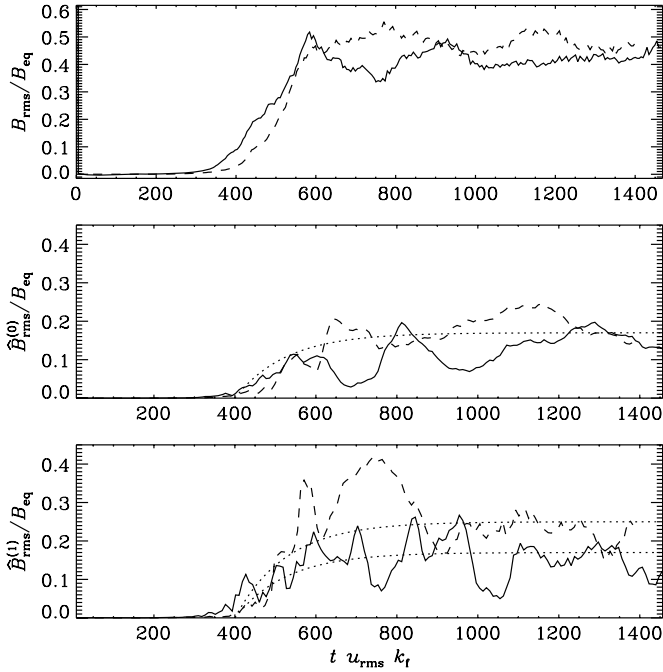


**Figure 12.** Top panel: rms values of the total magnetic field as functions of time for VF (Run B6, solid lines) and PC boundary conditions (Run B7, dashed lines). The two lower panels show the sums of the rms values of the Fourier amplitudes of  $B_x$  and  $B_y$  for  $k/k_1 = 0$  (middle panel) and  $k/k_1 = 1$  (bottom panel). The dotted lines in the two lower panels show a saturation predictor according to the model of Brandenburg (2001).

$Co \approx 0.3, \dots, 1.2$ , whereas for  $Co \approx 3.3$  the positive region in the top half of the convectively unstable layer disappears giving nearly zero value. For the most rapid rotation,  $Co \approx 8.7$ ,  $\alpha$  is negative in the whole convection zone. At first sight this result seems to contradict the corresponding results of Paper II, but we find that there is a qualitative change in the behavior of  $\alpha$  in the rapid rotation regime when the fluid Reynolds number is increased. For  $Re \approx 2$  there is no sign change and a monotonously increasing magnitude whereas for  $Re \approx 7$  the positive region in the upper layers of the convectively unstable layer disappears. Increasing the Reynolds number further to roughly 30 gives the result shown in Figure 13. We note that controlling  $Re$  and  $Co$  a priori is difficult in the rapid rotation regime because convection is increasingly suppressed especially for small Reynolds numbers.

For the slowest rotation, the turbulent pumping,  $\gamma$ , is very similar in profile and magnitude as in Paper II. In the case of  $\gamma$ , the behavior seems again different with negative values in the whole convection zone for  $Co \gtrsim 1.17$ . The magnitude of  $\gamma$  is significantly decreased for our case with the most rapid rotation. The turbulent diffusivity is rotationally quenched similarly as in Paper II. Also the coefficient  $\delta$  behaves in a similar fashion as in Paper II.

The relatively unchanged magnitude of  $\alpha$  and the significantly reduced value of  $\eta_t$  suggests that excitation of a mean-field dynamo could be possible in our cases with the most rapid rotation. One way to quantify this is to compute a local dynamo number

$$c_\alpha(z) = \frac{\alpha}{\eta_T k_f}, \quad (23)$$

where  $\eta_T = \eta_t + \eta$ . The results are shown in Figure 14. We find that the dynamo number peaks in the overshoot layer just below  $z/d = 0$  because the profile of the  $\alpha$ -effect extends somewhat

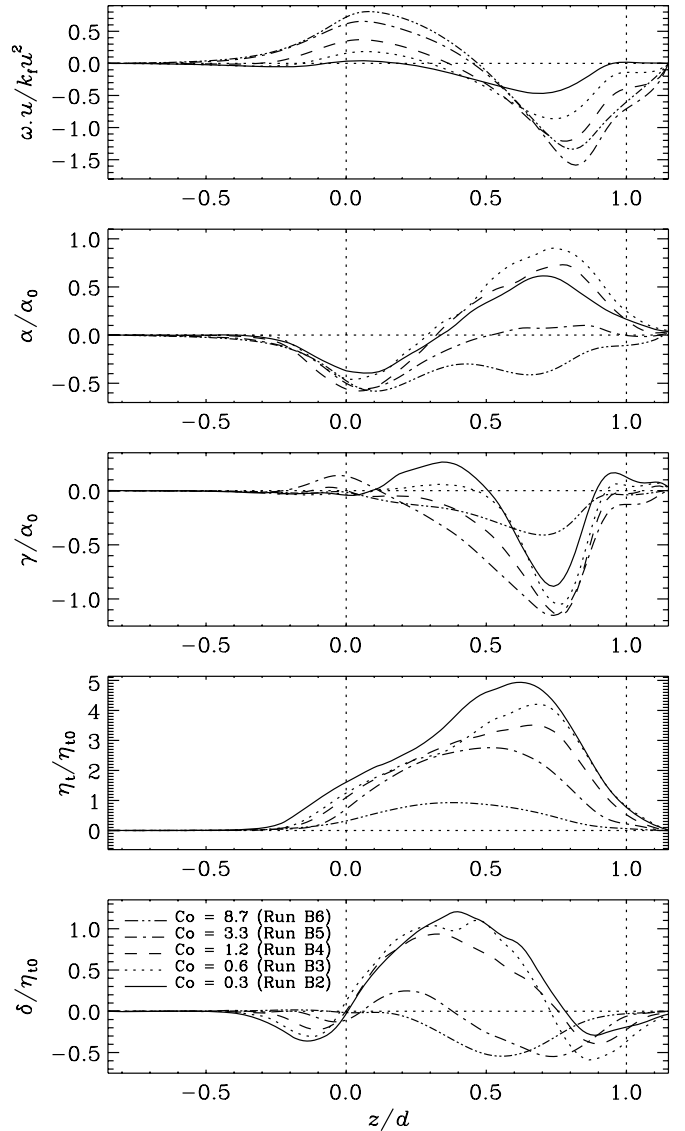


**Figure 13.** From top to bottom: normalized profiles of kinetic helicity,  $\alpha$ ,  $\gamma$ ,  $\eta_t$ , and  $\delta$  from kinematic test field simulations. The vertical dotted lines at  $z/d = 0$  and  $z/d = 1$  indicate the base and top of the convectively unstable layer, respectively.

deeper than that of turbulent diffusivity. The magnitude of the maximum of  $c_\alpha$  in the overshoot increases monotonically until  $Co \approx 3.3$  but the value in the convectively unstable layer remains small. For the most rapidly rotating case,  $c_\alpha(z)$  increases significantly also in the convectively unstable region due to the rotationally quenched value of  $\eta_t$ . In the homogeneous case, where  $c_\alpha$  is constant, dynamo action is possible when its value based on the lowest wavenumber in the domain exceeds unity, i.e.,  $C_\alpha \equiv c_\alpha k_f L_z / 2\pi > 1$ . In our case, owing to the presence of the overshoot layers,  $k_f L_z / 2\pi = 2$ , so one might expect that dynamo action is possible when the average value of  $c_\alpha(z)$  exceeds 0.5. For our case with the largest rotation rate this is clearly the case for most of the domain. We can therefore conclude that dynamo action should be possible in that case. However, a more detailed comparison would require using test fields with wavenumbers other than  $k = k_1$ , as was done in Paper II for a case with slower rotation than here. We should therefore not overinterpret our present comparisons.

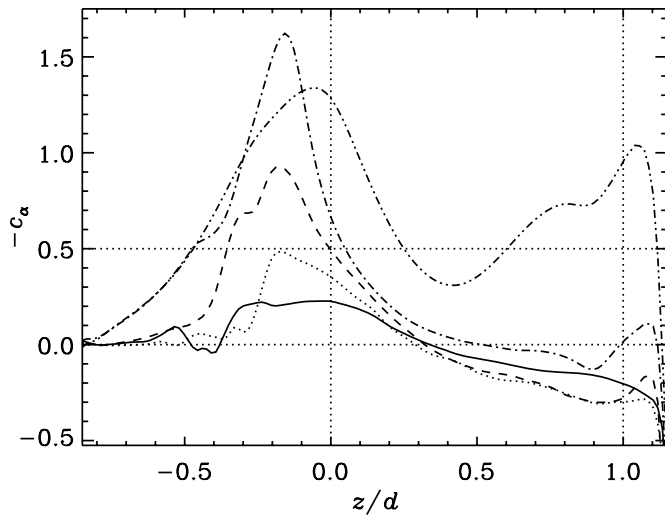


**Figure 14.** Vertical profiles of  $c_\alpha(z)$  for the same runs as in Figure 13. The horizontal line at  $-c_\alpha = 0.5$  denotes where  $|C_\alpha| = |c_\alpha|k_\Gamma L_z/2\pi = 1$ .

The significance of an overshoot layer in connection with large-scale dynamo action is not yet entirely clear. Tobias et al. (2008) argue that its presence is unimportant for promoting the generation of large-scale fields, while Browning et al. (2006) find it to be crucial. However, as discussed in the present paper, the rotation rate used in Tobias et al. (2008) may be too slow for a successful large-scale dynamo. Another issue might be the absence of shear-induced helicity fluxes (Vishniac & Cho 2001), as discussed in Paper I. In Browning et al. (2006), on the other hand, the presence of shear in the overshoot layer plays an important role, as is demonstrated by the striking difference to earlier results of Brun et al. (2004) without overshoot. Another aspect of the problem is that in local convection simulations the amount of overshoot decreases as rotation increases (Ziegler & Rüdiger 2003; Käpylä et al. 2004).

### 3.4. Mean-Field Models

In order to check how well the turbulent transport coefficients presented in the previous section describe the excitation of large-scale dynamos in the direct simulations, we use a one-dimensional mean-field dynamo model in which the test-field results for  $\alpha_{ij}$  and  $\eta_{ij}$  are used as input parameters. The model solves the equation

$$\dot{\bar{A}}_i = \alpha_{ij} \bar{B}_j - (\eta_{ij} + \eta \delta_{ij}) \mu_0 \bar{J}_j, \quad (24)$$

where the dot refers to a time derivative. The mean magnetic field and current density are given by  $\bar{\mathbf{B}} = (-\bar{A}'_y, \bar{A}'_x, 0)$  and  $\mu_0 \bar{\mathbf{J}} = -\bar{A}''_z$ , respectively. Here, primes denote  $z$ -derivatives.

The test-field results for  $\alpha_{ij}$  and  $\eta_{ij}$  can now be directly used in the mean-field model, leaving little freedom. We must, however, bear in mind the limitations of this simple model. First, the transport coefficients were determined for a single value of  $k$ , whereas in the direct simulations a larger set of wavenumbers are available. Second, the model is restricted to fields that depend only on  $z$ , whereas the direct simulations indicate that the large-scale field can also vary in the horizontal directions.

Nevertheless, it is interesting to study whether the transport coefficients derived using the test field procedure can excite a dynamo in the present case. The results for the growth rate  $\lambda$  of the magnetic field from the mean-field models, using the

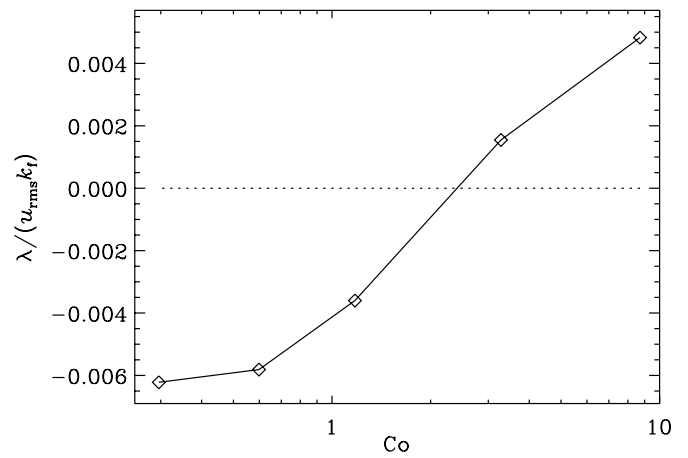


**Figure 15.** Growth rate of the large-scale magnetic field for the same runs as in Figure 13 from the one-dimensional dynamo model.

coefficients shown in Figure 13, are shown in Figure 15. We find that the two most rapidly rotating runs show clear dynamo action which is consistent with the direct simulations. These results support the notion that the mechanism generating the large-scale magnetic fields in the direct simulations is the turbulent  $\alpha$ -effect.

It should be noted that for values of  $\lambda$  different from zero the actual growth rate will not be exactly equal to  $\lambda$ , because in general the components of  $\alpha_{ij}$  and  $\eta_{ij}$  depend on frequency (and thereby on  $\lambda$ )—just as they also depend on the value of  $k$ ; see Hubbard & Brandenburg (2009) for details.

## 4. CONCLUSIONS

We use numerical simulations to demonstrate that rigidly rotating convection can generate a large-scale dynamo. The importance of this result lies in the fact that, according to mean-field theory, rotating turbulent convection leads to an  $\alpha$ -effect, which should result in a large-scale dynamo. So far this has not been seen in simulations without shear, leading to doubts of the applicability of the mean-field approach. The present results show that the lack of large-scale dynamos in rotating convection previously reported is probably due to too slow rotation. We find that an appreciable large-scale field is generated in the direct simulations if  $Co \gtrsim 4$ .

With the smallest system size explored here, the scale separation is small even in the most rapidly rotating case (Run A6), i.e.,  $k_{\max}/k_1 \approx 2$ . In this case, the large-scale magnetic field is concentrated in the  $k = 0$  mode. Doubling the domain size increases the scale separation to  $k_{\max}/k_1 \approx 5$  (Run B6). Here, the  $k = 0$  contribution is smaller and most of the magnetic energy is found for  $k/k_1 = 1$  and 2 modes. Doubling the size of the box once more,  $k_{\max}/k_1 \approx 10$ . The magnetic energy peaks at the largest scales, although the  $k = 0$  mode is significantly weaker than in the cases with smaller system sizes. This suggests that for the present parameters there is a maximum size for the large-scale magnetic field structures which is larger than  $2d$  and smaller than  $4d$ .

We compute the turbulent transport coefficients using the test field method and find that the magnitude of the  $\alpha$ -effect remains relatively unaffected when rotation increases. However, at the same time the turbulent diffusion is severely quenched by the rotation. When these coefficients are used in a one-dimensional mean-field dynamo model, the two most rapidly rotating runs exhibit a growing dynamo in accordance with the

direct simulations. Although the mean-field model is too simple to fully describe the field in the direct simulations, our results seem to validate the test field method further and lend support to our interpretation that the large-scale magnetic fields observed in the simulations are due to a turbulent  $\alpha$ -effect.

On a more general note, the present results also represent a nice demonstration of the usefulness of mean-field theory as a predictive tool. In fact, as explained in Section 3.2, our work was motivated by the earlier findings of Paper II that the  $\alpha$ -effect increases and the turbulent diffusivity decreases as the rotation rate is increased. This did already suggest the existence of an  $\alpha^2$ -dynamo for sufficiently rapid rotation—a suggestion that we have now been able to confirm in this paper.

It should be noted that the magnetic field structure of mean-field dynamos depends crucially on the geometry of the domain and the nature of the boundary conditions. Therefore, our results are not directly relevant to astrophysical bodies, because their geometry is not Cartesian nor the boundaries periodic. Our models can also not be thought of as local representations of a star, although it is possible to get some idea about the dependence of the transport coefficients on latitude (Ossendrijver et al. 2002; Käpylä et al. 2006; Paper II). Furthermore, the values of the magnetic Reynolds number are obviously not in the astrophysically relevant regime. Nevertheless, our simulations provide the first concrete evidence of dynamo action from rotating convection without the additional help of shear. This is an important point, because it proves for the first time that an  $\alpha^2$ -dynamo from rotating convection exists and that it is strong enough to produce large-scale fields. This was thought impossible until now (Cattaneo & Hughes 2006; Hughes & Cattaneo 2008; Hughes & Proctor 2009).

The anonymous referee is acknowledged for the detailed comments. The computations were performed on the facilities hosted by CSC-IT Center for Science Ltd. in Espoo, Finland, who are administered by the Finnish Ministry of Education. This research has benefited from the computational resources granted by the CSC to the grand challenge project “Dynamo08.” Financial support from the Academy of Finland grants 121431 (P.J.K.) and 112020 (M.J.K.) and the Swedish Research Council grant 621-2007-4064 (A.B.) is acknowledged. The authors acknowledge the hospitality of Nordita during the program “Turbulence and Dynamos” during which this work was initiated.

## REFERENCES

- Brandenburg, A. 2001, *ApJ*, **550**, 824
- Brandenburg, A., Bigazzi, A., & Subramanian, K. 2001, *MNRAS*, **325**, 685
- Brandenburg, A., Chan, K. L., Nordlund, Å., & Stein, R. F. 2005, *Astron. Nachr.*, **326**, 681
- Brandenburg, A., Jennings, R. L., Nordlund, Å., Rieutord, M., Stein, R. F., & Tuominen, I. 1996, *J. Fluid Mech.*, **306**, 325
- Brandenburg, A., & Käpylä, P. J. 2007, *New J. Phys.*, **9**, 305
- Brandenburg, A., Nordlund, Å., Pulkkinen, P., Stein, R. F., & Tuominen, I. 1990, *A&A*, **232**, 277
- Brandenburg, A., Rädler, K.-H., Rheinhardt, M., & Käpylä, P. J. 2008, *ApJ*, **676**, 740
- Brown, B. P., Browning, M. K., Brun, A. S., Miesch, M. S., Nelson, N. J., & Toomre, J. 2007, in *AIP Conf. Proc.* 948, *Unsolved Problems in Stellar Physics: A Conf. in Honor of Douglas Gough*, ed. R. J. Stancliffe et al. (New York: AIP), 271
- Browning, M. K., Miesch, M. S., Brun, A. S., & Toomre, J. 2006, *ApJ*, **648**, L157
- Brun, A. S., Miesch, M. S., & Toomre, J. 2004, *ApJ*, **614**, 1073
- Cattaneo, F., & Hughes, D. W. 2006, *J. Fluid Mech.*, **553**, 401
- Giesecke, A., Ziegler, U., & Rüdiger, G. 2005, *Phys. Earth Planet. Inter.*, **152**, 90
- Hall, D. S. 1991, in *The Sun and Cool Stars: Activity, Magnetism, Dynamos*, *Lecture Notes in Physics*, Vol. 380, ed. I. Tuominen, D. Moss, & G. Rüdiger (Berlin: Springer-Verlag), 353
- Hubbard, A., & Brandenburg, A. 2009, *ApJ*, submitted (arXiv:0811.2561)
- Hughes, D. W., & Cattaneo, F. 2008, *J. Fluid Mech.*, **594**, 445
- Hughes, D. W., & Proctor, M. R. E. 2009, *Phys. Rev. Lett.*, **102**, 044510
- Jones, C. A., & Roberts, P. H. 2000, *J. Fluid Mech.*, **404**, 311
- Käpylä, P. J., & Brandenburg, A. 2009, *ApJ*, in press (arXiv:0810.2298)
- Käpylä, P. J., Korpi, M. J., & Brandenburg, A. 2008, *A&A*, **491**, 353
- Käpylä, P. J., Korpi, M. J., & Brandenburg, A. 2009, *A&A*, in press (arXiv:0812.1792)
- Käpylä, P. J., Korpi, M. J., Ossendrijver, M., & Stix, M. 2006, *A&A*, **455**, 401
- Käpylä, P. J., Korpi, M. J., & Tuominen, I. 2004, *A&A*, **422**, 793
- King, E. M., Stellmach, S., Noir, J., Hansen, U., & Aurnou, J. M. 2009, *Nature*, **457**, 301
- Kleeorin, N., & Rogachevskii, I. 2008, *Phys. Rev. E*, **77**, 036307
- Krause, F., & Rädler, K.-H. 1980, *Mean-Field Magnetohydrodynamics and Dynamo Theory* (Oxford: Pergamon)
- Mitra, D., Käpylä, P. J., Tavakol, R., & Brandenburg, A. 2009a, *A&A*, **495**, 1
- Mitra, D., Tavakol, R., Brandenburg, A., & Moss, D. 2009b, *ApJ*, in press (arXiv:0812.3106)
- Mitra, D., Tavakol, R., Käpylä, P. J., & Brandenburg, A. 2009c, *Phys. Rev. Lett.*, submitted (arXiv:0901.2364)
- Moffatt, H. K. 1978, *Magnetic Field Generation in Electrically Conducting Fluids* (Cambridge: Cambridge Univ. Press)
- Nordlund, Å., et al. 1992, *ApJ*, **392**, 647
- Ossendrijver, M., Stix, M., & Brandenburg, A. 2001, *A&A*, **376**, 726
- Ossendrijver, M., Stix, M., Rüdiger, G., & Brandenburg, A. 2002, *A&A*, **394**, 735
- Parker, E. N. 1955, *ApJ*, **122**, 293
- Parker, E. N. 1979, *Cosmical Magnetic Fields: Their Origin and Their Activity* (Oxford: Clarendon)
- Proctor, M. R. E. 2007, *MNRAS*, **382**, 39
- Rogachevskii, I., & Kleeorin, N. 2003, *Phys. Rev. E*, **68**, 036301
- Rogachevskii, I., & Kleeorin, N. 2004, *Phys. Rev. E*, **70**, 046310
- Rotvig, J., & Jones, C. A. 2002, *Phys. Rev. E*, **66**, 056308
- Rüdiger, G., & Hollerbach, R. 2004, *The Magnetic Universe* (Weinheim: Wiley-VCH)
- Rüdiger, G., & Kitchatinov, L. L. 2006, *Astron. Nachr.*, **327**, 298
- Schekochihin, A. A., et al. 2009, *Phys. Rev. Lett.*, submitted (arXiv:0810.2225)
- Schrinner, M., et al. 2005, *Astron. Nachr.*, **326**, 245
- Schrinner, M., et al. 2007, *Geophys. Astrophys. Fluid Dyn.*, **101**, 81
- Sridhar, S., & Subramanian, K. 2009, *Phys. Rev. E*, in press (arXiv:0812.3269)
- Steenbeck, M., & Krause, F. 1969, *Astron. Nachr.*, **291**, 49
- Subramanian, K., & Brandenburg, A. 2006, *ApJ*, **648**, L71
- Sur, S., Brandenburg, A., & Subramanian, K. 2008, *MNRAS*, **385**, L15
- Tobias, S. M., Cattaneo, F., & Brummell, N. H. 2008, *ApJ*, **685**, 596
- Vishniac, E. T., & Brandenburg, A. 1997, *ApJ*, **475**, 263
- Vishniac, E. T., & Cho, J. 2001, *ApJ*, **550**, 752
- Yousef, T. A., et al. 2008a, *Phys. Rev. Lett.*, **100**, 184501
- Yousef, T. A., et al. 2008b, *Astron. Nachr.*, **329**, 737
- Ziegler, U., & Rüdiger, G. 2003, *A&A*, **401**, 433